Solution-Processed Zinc Phosphide (α-Zn_3P_2) Colloidal Semiconducting Nanocrystals for Thin Film Photovoltaic Applications

Erik J. Luber,[*,†,‡] **Md Hosnay Mobarok,**[†,‡] **and Jillian M. Buriak**[†,‡,*]

[†]National Institute for Nanotechnology (NINT), National Research Council, 11421 Saskatchewan Drive, Edmonton, Alberta T6G 2M9, Canada, and [‡]Department of Chemistry, University of Alberta, Edmonton, Alberta T6G 2G2, Canada

ABSTRACT Zinc phosphide (Zn_3P_2) is a promising earth-abundant material for thin film photovoltaic applications, due to strong optical absorption and near ideal band gap. In this work, crystalline zinc phosphide nanoparticles are synthesized using dimethylzinc and tri-*n*-octylphosphine as precursors. Transmission electron microscopy and X-ray diffraction data show that these nanoparticles have an average diameter of ~8 nm and adopt the crystalline structure of tetragonal α-Zn_3P_2. The optical band gap is found to increase by 0.5 eV relative to bulk Zn_3P_2, while there is an asymmetric shift in the conduction and valence band levels. Utilizing layer-by-layer deposition of Zn_3P_2 nanoparticle films, heterojunction devices consisting of ITO/ZnO/Zn_3P_2/MoO_3/Ag are fabricated and tested for photovoltaic performance. The devices are found to exhibit excellent rectification behavior (rectification ratio of 600) and strong photosensitivity (on/off ratio of ~10^2). X-ray photoelectron spectroscopy and ultraviolet photoemission spectroscopy analyses reveal the presence of a thin 1.5 nm phosphorus shell passivating the surface of the Zn_3P_2 nanoparticles. This shell is believed to form during the nanoparticle synthesis.

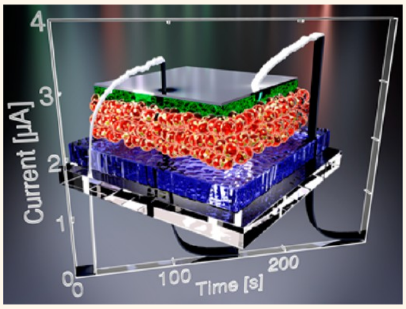

KEYWORDS: zinc phosphide · semiconductor nanocrystals · photovoltaics · quantum confinement · heterojunction · core–shell · solution-processed · earth-abundant

Solution-processed inorganic semiconductor nanocrystals are becoming increasingly attractive components in photovoltaic applications due to the ability to tune optical and electrical properties,[1−5] compatibility with flexible electronics,[6,7] and large-area low-cost fabrication.[8,9] Because of their exceptional performance in photovoltaic applications, both lead chalcogenide PbX (X = S, Se)[10−15] and cadmium chalcogenide CdX (X = S, Se, Te)[16−20] nanocrystals have received considerable attention. However, extensive effort is being made to develop alternative semiconducting nanocrystalline materials which use nontoxic precursors that are earth-abundant,[21] such as Cu_xS,[22−25] and FeS_2,[26−28] but have thus far shown limited photovoltaic power conversion efficiencies.

Zinc phosphide (Zn_3P_2) is a particularly promising candidate material for photovoltaic applications due to its near ideal direct optical band gap of 1.5 eV,[29] large optical absorption coefficient ($>10^4$ cm^{-1}),[29,30] long minority-carrier diffusion lengths (5−10 μm),[31] and large range of doping concentrations (10^{13}−10^{18} cm^{-3}).[32] In addition, zinc phosphide has been identified as having the necessary photovoltaic and economic characteristics to be broadly used as a solar cell material.[21] Impressive photovoltaic performance has been demonstrated in Zn_3P_2/Mg Schottky diode cells, with reported power conversion efficiencies (PCE) ranging from 4.5%[32] to 6%,[33] while Zn_3P_2/ZnO heterojunctions with PCEs of 2% have been achieved.[34] All the reported zinc phosphide solar cell devices, however, have used Zn_3P_2 wafers or polycrystalline films, which require high temperature thermal annealing[32,33] (>850 °C), vacuum deposition,[34] or metalorganic chemical vapor deposition methods.[35]

Zinc phosphide nanostructures have been reported, including nanowires,[36−40] nanobelts,[41,42] nanotubes,[43] to nanotrumpets.[44]

* Address correspondence to
eluber@ualberta.ca,
jburiak@ualberta.ca.

Received for review July 5, 2013
and accepted August 12, 2013.

10.1021/nn4034234

These structures have not been screened for solar cell applications, presumably due to the difficulty of fabricating large area and compact films of desired thicknesses. The synthesis of zinc phosphide nanoparticles has previously been reported,[45−47] however crystallographic X-ray diffraction (XRD) investigations revealed a lack of obvious crystalline phases or were not performed. Here we report the synthesis of crystalline Zn_3P_2 colloidal nanoparticles, the crystallinity of which is clearly demonstrated by XRD and electron microscopy. Using ligand exchange or thermal annealing, thin films of Zn_3P_2 nanocrystals of controllable thicknesses were prepared and analyzed. Critical to device integration are the optical and electronic properties of these nanocrystalline Zn_3P_2 thin films, which were determined using UV−vis spectroscopy and ultraviolet photoemission spectroscopy (UPS). On the basis of these results, ZnO/Zn_3P_2 heterojunction photodiodes were fabricated and tested under AM 1.5G illumination, which displayed excellent rectification behavior and photoconductivity.

RESULTS AND DISCUSSION

Zn_3P_2 Nanoparticle Synthesis. A number of recent investigations have demonstrated that tri-*n*-octylphosphine (TOP) can act as a phosphorus source for the synthesis of metal phosphide nanostructures at high reaction temperatures.[48,49] For instance, copper phosphide,[50] nickel phosphide,[51−53] cobalt phosphide,[54] iron phosphide,[55,56] and indium phosphide[57] have been successfully prepared and characterized. The chemistry described here to prepare solution-dispersible Zn_3P_2 crystalline nanoparticles (NP) is straightforward, and uses a hot injection solution phase approach,[48,49] with dimethylzinc as the zinc source, and TOP as a phosphorus source and a surface-passivating ligand.

Nanoparticle Characterization. Shown in Figure 1a is a transmission electron micrograph (TEM) of NPs from a typical batch of well-dispersed zinc phosphide NPs in *n*-octane. The nanoparticles are observed to have a generally spherical shape with slight irregularities. The inset in Figure 1a is a histogram of the measured particle diameters, which were found to be log-normally distributed with an average size of 9 nm and a standard deviation of 3 nm. The presence of several distinct rings in the selected area electron diffraction (SAED) pattern in Figure 1b clearly demonstrates the crystallinity of the NPs. Moreover, the measured SAED ring pattern is found to be in excellent agreement with the simulated ring pattern for α-Zn_3P_2, both in relative intensity and *d*-spacing ratios. From high-resolution TEM analysis of the zinc phosphide NPs (Figure 1c) lattice fringes are clearly identifiable, showing that the individual NPs are crystalline.

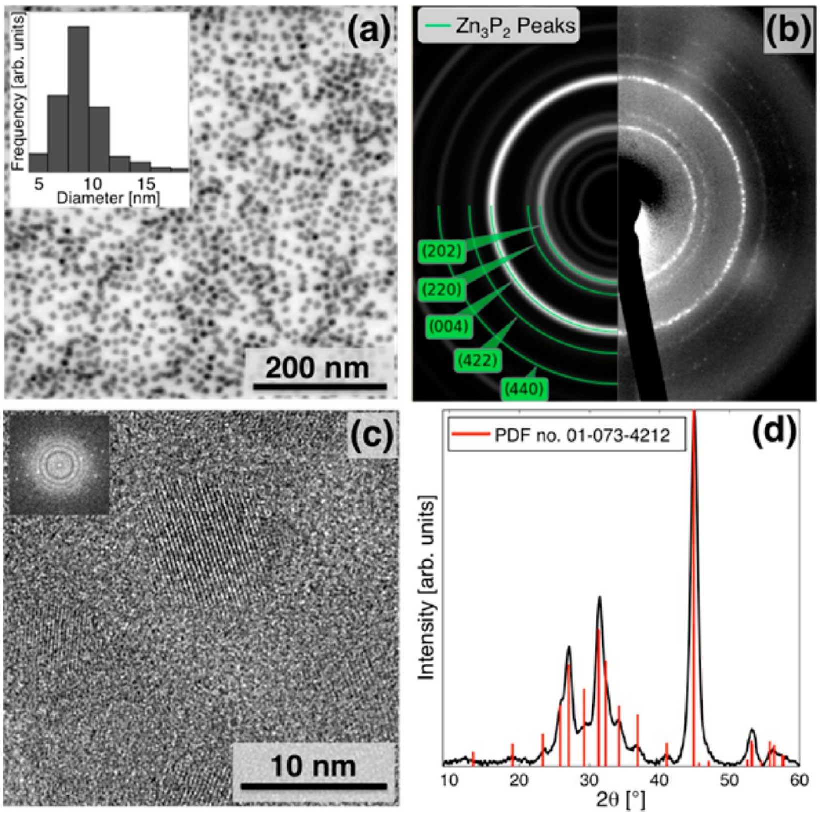

Figure 1. (a) TEM micrograph of Zn_3P_2 nanoparticles (inset: particle size distribution). (b) Selected area diffraction pattern of Zn_3P_2 nanoparticles (right) and simulated ring pattern (left). (c) High-resolution TEM micrograph of Zn_3P_2 nanoparticles (inset: FFT diffractogram). (d) XRD pattern of Zn_3P_2 nanoparticles and bulk diffraction pattern of Zn_3P_2 (PDF no. 01-073-4212).

X-ray diffraction (XRD) characterization of the zinc phosphide NPs in Figure 1d reveals a series of broad crystalline reflections, which are found to correspond to that of bulk tetragonal Zn_3P_2 (PDF no. 01-073-4212). Lattice constants of a = 8.06 and c = 11.38 Å are obtained by determining the peak centroids of the (004) and (400) reflections and using the relation $1/d_{hkl} = ((h^2 + k^2)/a^2 + l^2/c^2)^{1/2}$, where d_{hkl} is the plane spacing of an (hkl) reflection. These values agree very well with the lattice constants of a = 8.08 and c = 11.40 Å for bulk Zn_3P_2. Furthermore, these data indicate that no other crystalline phases are present, since all observed reflections could be accounted for by the Zn_3P_2 phase. The average crystallite diameter (D), was determined by the Scherrer relation,[58] $D = K_s\lambda/(\beta \sin(\theta))$, where K_s = 1.07 for spherical crystallites, λ is the X-ray wavelength, β is the integral breadth of a given peak, and θ is the corresponding peak centroid. Application of this relation to the most intense reflection (004), the average crystallite size is found to be 7.6 nm, which agrees reasonably well with the sizes observed in TEM.

Film Deposition. The ability to tune the layer thicknesses of semiconductor nanoparticle photovoltaic devices is a critical requirement to achieve optimal performance.[18,59] As such, a layer-by-layer (LbL) approach was adapted for the deposition of Zn_3P_2 NP thin films.[60] All films were deposited and processed in a nitrogen-filled glovebox, unless otherwise noted. It is generally found that removal or exchange of the long-chain coordinating ligands of semiconducting nanoparticles is necessary for efficient charge transport in NP films.[61−64] To this end, a solid-state ligand exchange was attempted by treating the films with 1,2-ethanedithiol (EDT) (see Methods section). Shown in Figure 2a is the transmission FTIR spectrum of a single layer film consisting of as-deposited Zn_3P_2 NPs on double-side polished silicon. The as-deposited film shows strong absorption from five different C−H stretching modes (n = 2954, 2925, 2901, 2870, and 2853 cm^{-1}), consistent with the presence of TOP capping ligands (see Supporting Information, Figure S1 for FTIR spectrum of free TOP). Treatment of these Zn_3P_2 NPs with EDT, as described above, results in a ~35% reduction in signal from the C−H stretching region (see inset Figure 2a), which suggests partial displacement of the TOP ligands. This partial ligand removal allowed for subsequent layers to be deposited in an LbL fashion, without redissolution of previous layers. Several attempts were made to utilize other ligands, such as 3-mercaptopropionic acid (MPA) or pyridine, which also resulted in partial removal of the TOP ligands, but was found to visibly attack the film surface.

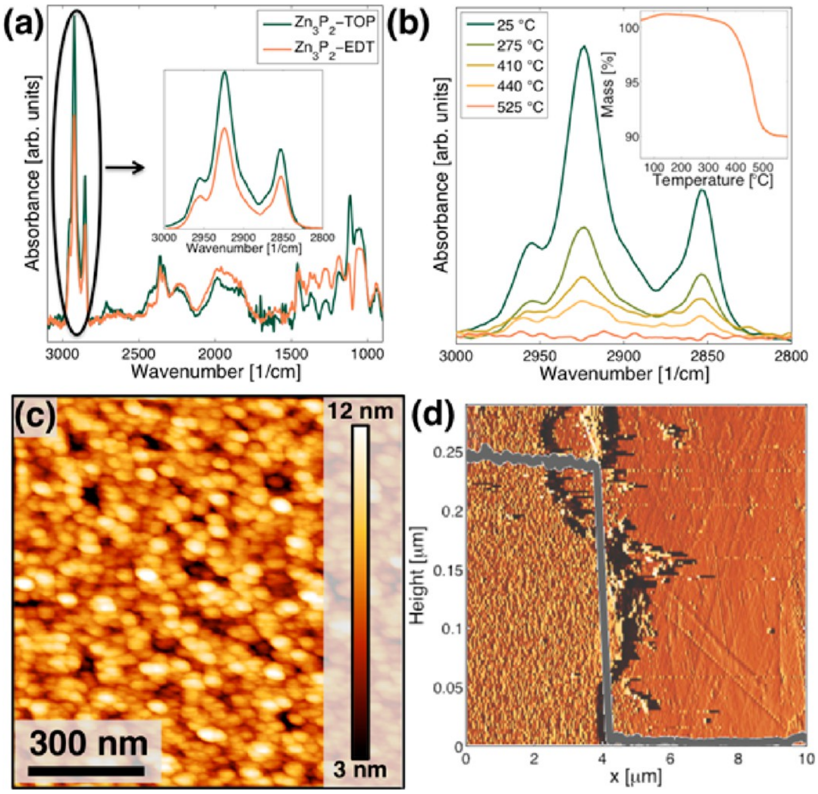

Figure 2. FTIR spectra of Zn_3P_2 NP films (a) following solid-state EDT treatment (inset: zoomed in view of C−H_x stretch region) and (b) thermal treatments ranging from room temperature to 525 °C (inset: TGA analysis of Zn_3P_2 NPs capped with native TOP ligands). (c) AFM micrograph of Zn_3P_2 NP film deposited using thermal LbL processing (15 layers thick) and (d) corresponding height profile from a scratch for a thickness measurement, revealing an average thickness of 240 ± 6 nm.

Owing to the insulating nature of bulky long-chain TOP ligands, an alternative LbL method was employed, where the native ligands were removed *via* thermal annealing cycles (see Methods section). Shown in Figure 2b are the transmission FTIR spectra of Zn_3P_2 NP films on double-side polished Si, annealed in a nitrogen-filled glovebox at temperatures ranging from room temperature to 525 °C. The quantity of ligand removed increases with annealing temperature, but complete removal does not occur until temperatures are in excess of 500 °C. This result agrees well with the thermogravimetric analysis (TGA) of Zn_3P_2 NPs shown in the inset of Figure 2b, where a broad weight loss event begins at ~250 °C and ends at ~500 °C, which is attributed to the loss of coordinating TOP. As such, all films deposited using thermal processing were annealed at 525 °C to ensure that all of the coordinating ligand was removed. Unless otherwise stated, all films in this study were deposited *via* thermal annealing LbL. An atomic force microscope (AFM) height map of the surface of a Zn_3P_2 NP thin film is shown in Figure 2 panels c and d; this film was deposited *via* 15 thermal annealing LbL cycles. The film is a compact assembly of NPs, which is free of deep pinholes or cracks. Some nanoscale pinholes are visible on the surface (Figure 2c), but they are apparently filled in with each successive layer, since the surface shown in Figure 2d is extremely smooth with a root-mean-square roughness of 1.5 nm. The film thickness was measured at an edge created by scratching the film, as can be observed in Figure 2d. The film was found to be very uniform across the edge with a thickness of 240 ± 6 nm, which suggests that each individual layer was roughly 16 nm thick.

Electronic and Optical Properties. Knowledge of the electronic and optical parameters of zinc phosphide NPs is critical for rational design of photovoltaic device integration.[65] Optical absorption measurements of Zn_3P_2 NP thin films reveals the presence of both an indirect and direct band gap. An indirect band gap of 1.8 eV and a direct gap of 2.0 eV was obtained from the Tauc plots[66] (Figure 3a,b) using the relation $\alpha h\nu \propto (E_g - h\nu)^{1/n}$, where α is the optical absorption coefficient, $h\nu$ is the photon energy, E_g is the energy gap and $n = {}^1/_2$ for indirect transitions and $n = 2$ for direct transitions. Comparing these values with those of bulk Zn_3P_2, the indirect and direct optical band gaps were reported to be 1.3−1.4 eV[30,67] and 1.4−1.6 eV,[30,68] respectively. As such, there appears to be an upward shift of ~0.5 eV in both the indirect and direct band gaps. One plausible explanation for this large shift in band gap is due to quantum confinement in these nanoparticles.[69,70] Because of chemical and structural similarity with Cd_3P_2, which has a very large exciton Bohr radius of ~36 nm,[71,72] it is expected that Zn_3P_2 nanostructures would also be subject to such strong quantum confinement effects, which have been reported by several authors.[46,47] However, further studies investigating the dependence of band gap on the size of these Zn_3P_2 NPs are necessary to determine the origin of this 0.5 eV shift.

The valence photoemission and secondary electron spectra of Zn_3P_2 NP films are shown in Figure 3c. From the onsets of these spectra, the work function (ϕ), and ionization energy (IE) are found to be 4.35 and 5.15 eV, respectively. Using these values in conjunction with the optically derived band gap, an energy band diagram for these Zn_3P_2 NPs can be constructed, which is shown in Figure 3d. Several observations can be made when comparing the energy band diagrams of Zn_3P_2 NPs and bulk Zn_3P_2 (Figure 3e).[73,74] First, the Zn_3P_2 NPs have mild *p*-type doping, which is thermodynamically expected due to the equilibrium concentration of zinc vacancies and phosphorus interstitials.[73] Second, there is an asymmetric shift in the energy levels of the conduction band-edge minimum (CBM) and the valence band-edge maximum (VBM), where the CBM shifts upward by 0.35 eV and the VBM shifts downward by 0.15 eV. According to SEPM calculations and experimental determination of CBM and VBM shifts in a variety of quantum confinement of semiconductor nanocrystals,[70] there is typically an asymmetric shift, where the shift in CBM level is greater than that of the VBM level. As such, this result further validates that notion that these Zn_3P_2 NPs have shifted energy levels as a result of quantum confinement size effects.

Device Fabrication and Testing. To assess the applicability of Zn_3P_2 NPs for optoelectronic applications, a thin film device structure consisting of ITO/ZnO/Zn_3P_2 NPs/MoO_3/Ag was realized. Figure 4a outlines the flat-band energy levels (taken from literature[59,75,76] and this work) corresponding to such a device. ZnO, which is an *n*-type semiconductor,[77] is used as the electron acceptor, as it has previously been shown to be a suitable acceptor for bulk Zn_3P_2.[34] Moreover, ZnO is expected to form a type-II heterojunction with Zn_3P_2 NPs, which should assist in the charge separation of photogenerated excitons in the Zn_3P_2 NP layer. The ZnO film was spin-coated from a sol−gel[78] at 1500 rpm onto a precleaned ITO/glass substrate, which was then annealed at 100 °C for 15 min, followed by a 1 min anneal at 525 °C. From XRD analysis (see Supporting Information, Figure S2) the ZnO film was found to adopt a Wurtzite structure (a = 3.2 Å and c = 5.2 Å) and out-of-plane grain size greater than 60 nm. The Zn_3P_2 NP film was deposited on top of the ZnO film using the previously described thermal LbL process. Following Zn_3P_2 deposition, a 10 nm MoO_3 layer was deposited using thermal evaporation. In an architecture very similar to the one used in this work (ITO/ZnO/PbS NPs/MoO_3/anode), it has previously been demonstrated[59] that the MoO_3 layer pins the Fermi level of the anode, resulting in the formation of an ohmic contact with NPs and allowing for the use of low-work function

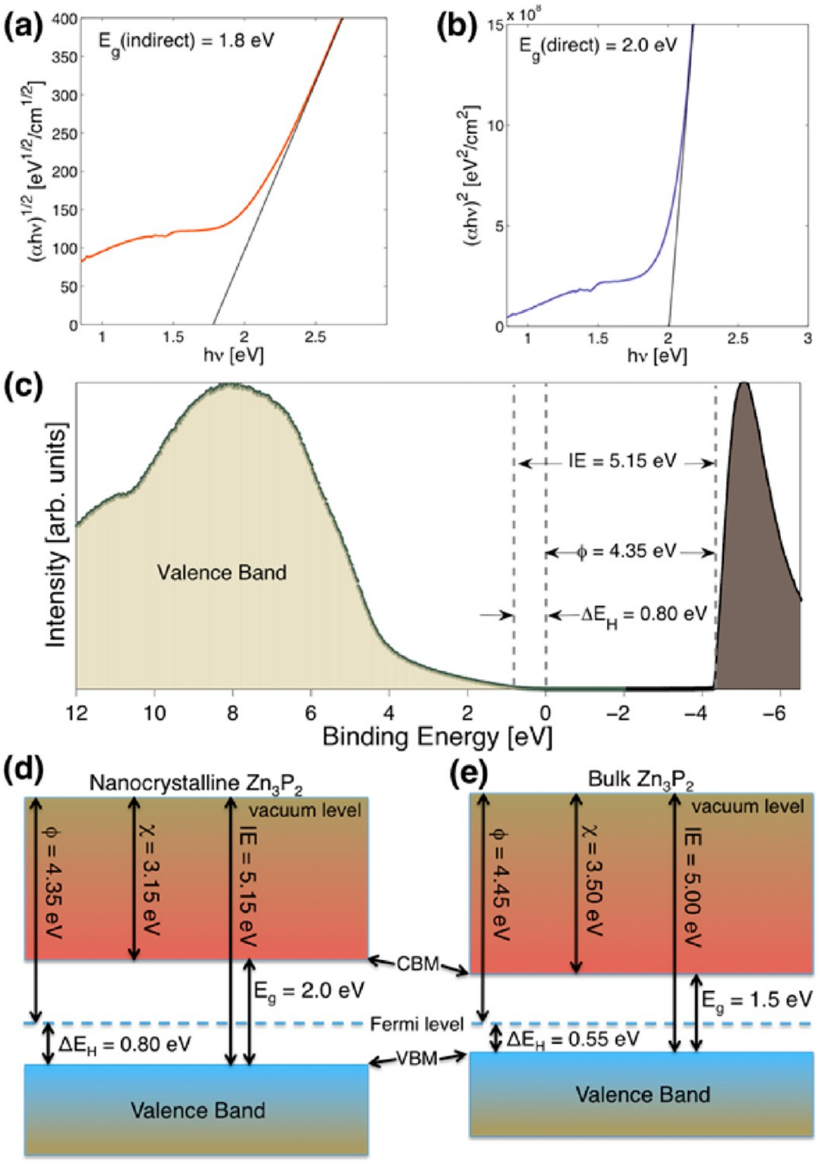

Figure 3. Optical absorption Tauc plots of zinc phosphide NP films for (a) indirect and (b) direct transitions. (c) Valence photoemission spectrum (left) and secondary electron spectrum (right) of Zn_3P_2 of NP films. Energy band diagrams of (d) nanocrystalline Zn_3P_2 and (e) bulk Zn_3P_2 (constructed using values taken from refs 70 **and** 71**).**

electrodes such as Ag. Moreover, a MoO_3 interfacial layer has been shown to be an effective electron-blocking/hole-transporting layer.[79,80] Lastly a 100 nm Ag top electrode was deposited *via* thermal evaporation.

Figure 4b shows the current−voltage (*J*−*V*) curves of a ITO/ZnO/100 nm Zn_3P_2 NP/MoO_3/Ag heterojunction device measured in the dark and under 100 mW/cm^2 AM 1.5G illumination. Importantly, we see that the Zn_3P_2 NP-based device exhibits a strong photoconductive effect, where the observed current under AM 1.5G illumination is much larger than in the dark. This increase in current is likely due to the photogenerated electron−hole pairs in the depleted Zn_3P_2 NP layer.[39] The inset in Figure 4b is the on/off ratio (ratio of measured current under illumination and the dark), which is found to be ∼10^2. This on/off ratio is significantly greater than unity, indicating these devices are quite sensitive to light. Moreover, this result compares favorably to previously fabricated ZnO/Zn_3P_2 single crystal nanowire heterojunction photodiodes,[39] where a maximum on/off ratio of ∼10^2 was obtained. To confirm that the observed photoconductivity of these devices was a result of the Zn_3P_2 NP film, control devices consisting of ITO/ZnO/MoO_3/Ag were fabricated, where a minimal photoresponse with an on/off ratio of ∼10^0 was measured (Supporting Information, Figure S3). Second, we see that the Zn_3P_2 heterojunction device exhibits excellent rectification behavior and low leakage currents, with a rectification ratio (current ratio at +1 V and −1 V in the dark) of ∼600. This compares well with other earth-abundant nanocrystalline semiconductor systems, such as thin film FeS_2 nanocrystal-based photodiodes,[28] where a rectification ratio of ∼500 was reported for optimized ITO/ZnO/FeS_2/MoO_3/Au devices. Lastly, the

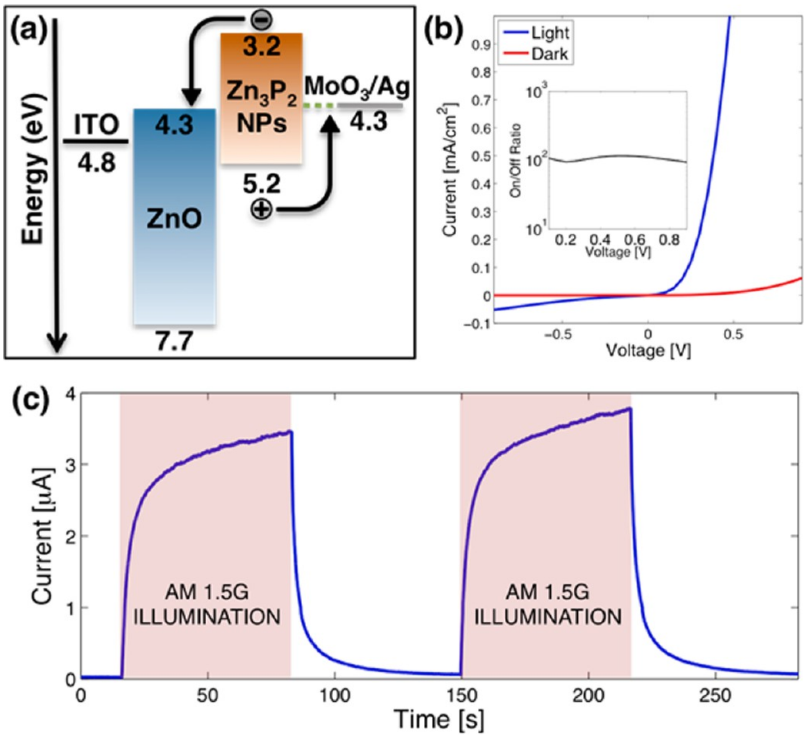

Figure 4. (a) Flat-band energy level diagram of an ITO/ZnO/Zn_3P_2 NP/MoO_3/Ag thin film heterojunction photovoltaic device. (b) Corresponding *J*−*V* curves of a ZnO/100 nm Zn_3P_2 NP heterojunction device measured in the dark (red) and under 100 mW/cm^2 AM 1.5G illumination (blue). (c) Photoresponse of ZnO/100 nm Zn_3P_2 NP heterojunction device under alternating cycles of dark and AM 1.5G illumination and a 0.5 V bias.

temporal photoresponse of the Zn_3P_2 heterojunction device under alternating cycles of AM 1.5G illumination and dark, is shown in Figure 4c. Upon switching on the AM 1.5G illumination there is a sharp rise in the current, and a sharp decrease when the illumination is turned off, which is repeatable over multiple switching cycles. The average response time of these devices was found to be ~5 s, which is similar to thin film FeS_2 nanocrystal photodiodes which exhibit a response time of ~20 s.[26]

Heterojunction devices of the same architecture were fabricated, where the Zn_3P_2 NP film was deposited using LbL EDT treatments. Photoconductivity and rectification were also observed in these devices (Supporting Information, Figure S4); however, lower on/off and rectifications ratio were obtained. Similar results were obtained for LbL EDT treated devices processed in atmospheric conditions. The reduced performance of the EDT treated Zn_3P_2 NP devices is likely due to the presence of the long chain TOP ligands, which are expected to significantly impede charge transport within the device.[61−64]

Nanoparticle Surface Characterization. Despite excellent photosensitivity and rectification behavior of the Zn_3P_2 NP heterojunction devices, no detectable short-circuit current was observed. This lack of short-circuit current could not be attributed to the insulating nature of coordinating ligands, since the thermally treated devices also failed to produce short-circuit currents. Moreover, electrical characterization of thermally treated Zn_3P_2 films revealed that the film resistivities were greater than 10^5 $\Omega\cdot$cm. This suggests that the lack of short-circuit current in the heterojunction devices is related to intrinsic properties of Zn_3P_2 NPs themselves.

From XRD and TEM characterization, it was found that the synthesized NPs consist of crystalline α-Zn_3P_2. However, the presence of thin layers of inorganic insulating species formed on the surface of the nanoparticles during synthesis would be difficult to detect using the aforementioned characterization techniques. As such, the surface chemistry of these NPs was investigated using X-ray photoelectron spectroscopy (XPS) and UPS. All films were prepared, loaded into the XPS/UPS sample holder, and sealed in a transport container, in a nitrogen-filled glovebox. The samples were then transferred to the XPS/UPS chamber, while exposure to atmosphere was minimized (~1 min).

The valence photoemission spectrum of a thermally treated Zn_3P_2 NP film is shown in Figure 3c. Previously, the valence photoemission spectrum of bulk Zn_3P_2 was studied,[74] and four distinct features were observed: (i) the Zn(3d) core level peak at 10 eV, (ii) a broad feature in the range of 9−7 eV, due to a P s-like band, (iii) a peak centered at 5 eV, which is a mix of P(3p) and Zn(4s) states and (iv) a long tail ranging from ~3.5 eV to the valence band maximum. The valence photoemission spectrum in Figure 3c clearly shows the Zn(3d) feature, the P s-like band and the long tail near the VBM.

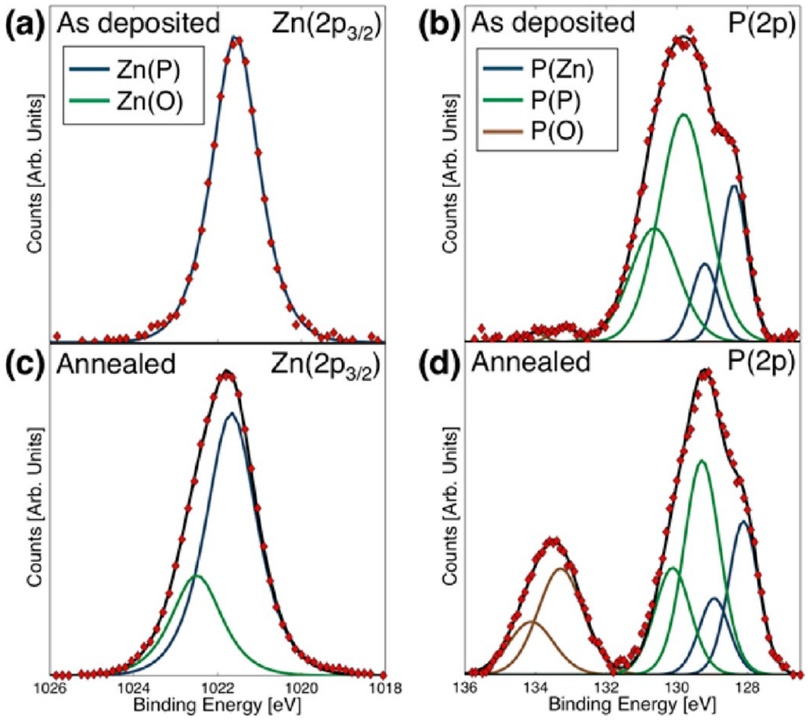

Figure 5. High-resolution XPS spectra of Zn_3P_2 NP films. As-deposited film (a) $Zn(2p_{3/2})$ region and (b) P(2p) region. Thermally annealed (525 °C) film (c) $Zn(2p_{3/2})$ region and (d) P(2p) region.

The peak centered at 5 eV is not as immediately obvious, but detailed inspection clearly reveals a shoulder of the main broad peak at ~5 eV. Upon comparison of the Zn_3P_2 NP and bulk Zn_3P_2 photoemission spectra, it is seen that the broad feature in the range of 9−7 eV is much more intense in NPs than in bulk specimens. As found previously for bulk Zn_3P_2,[74] a relative increase in the 9−7 eV feature is attributed to an increased concentration of phosphorus on the surface, as such, this data suggests that the surface of the Zn_3P_2 NPs are phosphorus-rich.

To further investigate the chemical composition of these films, X-ray photoelectron spectroscopy (XPS) was carried out. Figure 5 panels a and b show the high-resolution XPS spectra of the $Zn(2p_{3/2})$ and P(2p) regions of an as-deposited Zn_3P_2 NP film. The $Zn(2p_{3/2})$ spectrum is fit by a single peak centered at 1021.6 eV, which is attributed to Zn in Zn_3P_2.[81−83] The P(2p) region reveals a much more complex spectra, which is fit by a pair of doublets. The lowest binding energy doublet is attributed to P in Zn_3P_2,[81−83] where the first doublet peak is centered at 128.4 eV. Using the Zn(P) peak centered at 1021.6 eV and the P(Zn) doublet centered at 128.4 eV, the atomic concentrations of Zn(P) and P(Zn) species are calculated to be 58 atomic % Zn and 42 atomic % P, which is very close to the ideal stoichiometry of 60 atomic % Zn and 40 atomic % P for Zn_3P_2 crystals.

The second doublet found in the P(2p) spectra further substantiates the presence of another phosphorus-containing species on the surface of the NPs. The first peak of this doublet has a peak center of 129.8 eV, which is very close the to binding energy position of 129.7 eV of elemental red phosphorus,[84] suggesting this doublet is due to P−P bonding. This doublet is often found upon XPS analysis of bulk Zn_3P_2 surfaces, where some authors ascribe it to P−P bonding,[81,82] while others have attributed it to phosphorus suboxides.[85] Alternatively, this secondary doublet could also be due to the phosphorus−carbon bonds of the tri-*n*-octylphosphine ligands. If the TOP ligands are the source of this second doublet, then upon thermally annealing at 525 °C we would expect the doublet to disappear from the P(2p) spectrum since the FTIR results show the complete removal of TOP ligands following annealing at 525 °C. Inspection of the P(2p) spectrum of a thermally annealed Zn_3P_2 NP film (Figure 5d) clearly shows that this secondary doublet is still present, ruling out TOP ligands as the origin of this other phosphorus species on the surface.

From XRD analysis, it was found that the grain size of the Zn_3P_2 NP films remains relatively unchanged after annealing at 525 °C (see Supporting Information, Figure S5). This is surprising since Zn_3P_2 NP films are annealed at a temperature of $0.68T_m$,[86] and therefore, we would expect rapid diffusion and significant grain growth at these elevated temperatures, especially for a nanocrystalline film.[87] This result suggests that the Zn_3P_2 NPs have a core−shell-like structure, where the shell hinders atomic diffusion between neighboring Zn_3P_2 NPs. An insulating shell such as this could account for the large resistivity of the Zn_3P_2 films and explain the poor charge transport in the Zn_3P_2 NP films. However, it has previously been shown that the resistivity of bulk Zn_3P_2 can vary between 10 and 10^4 Ω·cm, due to varying levels of intrinsic charge carrier concentrations.[88] As such, further investigation into the mechanisms of electrical conduction in these Zn_3P_2 NP films is needed to elucidate the rate-limiting steps governing charge transport.

From XPS and XRD data, it is possible to roughly estimate the thickness of the shell structure. If we assume spherical particles and a phosphorus-rich shell with molar density, ρ_s, then the thickness of the shell, t, is given by (see Supporting Information for detailed derivation and calculations)

$$t = r\left(\sqrt{1+\frac{\rho_c A_s}{\rho_c A_s}-1}\right)$$

where r is the core radius, ρ_c is the molar density of phosphorus in the Zn_3P_2 core, A_s and A_c are the areas of the P(P) and P(Zn) doublets. From this relation, the shell thickness is estimated to ~1.5 nm.

Although the origin of this phosphorus-rich shell is not well understood at this point, it is instructive to analyze the various chemical steps that must occur during the synthesis procedure. The P atom in TOP starts out with a formal oxidation state of P^{3+}, but in Zn_3P_2, it has a charge of P^{3-}. As the TOP decomposes, it would be expected to pass through an intermediate oxidation state of P^0, which is obviously stable, since elemental phosphorus is highly abundant.

CONCLUSIONS

We have successfully developed a new synthetic method for the production of colloidal crystalline Zn_3P_2 nanoparticles. These NPs were found to be on the order of ~8 nm as characterized by various methods. Following this, two different layer-by-layer processes were developed for the deposition of Zn_3P_2 NP films of arbitrary thickness. From optical measurements, the indirect and direct band gaps of the Zn_3P_2 NPs were found to increase by 0.5 eV, compared to bulk Zn_3P_2. As determined by UPS, the NP films were found to have an asymmetrical shift of 0.35 and 0.15 eV in the CBM and VBM energy levels. From these optical and electronic structure measurements, it was proposed that these energy shifts are a result of quantum confinement size-related effects. Using LbL deposition of Zn_3P_2 NP films, heterojunction devices consisting of ITO/ZnO/Zn_3P_2 NPs/MoO_3/Ag were fabricated and tested. They were found to possess excellent rectification behavior (rectification ratio of ~600) and photosensitivity (on/off ratio of ~10^2 under 100 mW/cm^2 AM 1.5G illumination); however, the devices had zero short-circuit current. XPS and UPS analysis of the nanoparticle surfaces revealed the presence of a secondary phosphorus-containing species. It was postulated that a 1.5 nm thick insulating phosphorus-rich shell surrounds the Zn_3P_2 NPs, which could account for the lack of short-circuit current in the heterojunction devices. New synthetic methods are being developed for the production of Zn_3P_2 NPs that do not have an insulating phosphorus shell.

METHODS

Materials. Dimethylzinc (96%) was obtained from Alfa-aesar; tri-*n*-octylphosphine (97%) was obtained from Strem Chemicals and 1-octadecene (90%, technical grade) and MoO_3 (99.99%) were obtained from Sigma-Aldrich. All solvents were degassed and distilled before use. All reactions and postreaction processing were carried out under argon atmosphere using Schlenk techniques or in a glovebox, unless otherwise noted. Indium tin oxide (ITO) coated glass substrates (8−12 Ω/□) were purchased from Delta Technologies Ltd.

Zn_3P_2 NP Synthesis. In a typical experiment, a mixture of 1-octadecene (6−8 mL) and TOP (2 mL) were degassed *via* argon bubbling in a 3-neck flask (fitted with a reflux condenser) at an elevated temperature (~100 °C) for 1 h. The solution was heated to ~320 °C, followed by a rapid injection of dimethylzinc (diluted with 2 mL of TOP before injection). The solution temperature was raised to 350 °C over the subsequent 2 h, and the solution was allowed to stir at this temperature for another 3−4 h. Following this, the solution was transferred to a nitrogen-filled glovebox to wash the nanoparticles. The particles were isolated by the addition of toluene to the crude mixture, followed by filtration through 0.45 μm filter of the solution to remove larger aggregates. The addition of a minimal volume of 2-propanol led to the flocculation of particles, which were separated by centrifugation. This washing cycle was repeated at least three times to remove the excess TOP and 1-octadecene. The particles were then redispersed in either toluene or in *n*-octane for characterization and device fabrication.

Characterization. TEM characterization was carried out using a JEOL 2200 FS TEM/STEM microscope operating at an accelerating voltage of 200 kV. HRTEM imaging was performed on a Hitachi HF 3300 TEM/STEM, operating at an accelerating voltage of 300 kV. Samples were prepared by dipping ultrathin holey-carbon grids in a dilute solution of Zn_3P_2 NPs dispersed in toluene. The particle size distribution was determined using a thresholding algorithm, implemented in Gwyddion.[89] SAED patterns were analyzed using Diffraction Ring Profiler,[90] and the electron diffraction ring pattern was simulated in GDIS,[91] where the crystallographic positions for the unit cell were taken from Kloc *et al.*[92]

XRD characterization was carried out using a Bruker AXS D8 Discover diffractometer, equipped with an area detector and a Cu Kα radiation source (λ = 1.54056 Å). All samples were prepared by drop-casting from a concentrated solution (~40 mg/mL) of Zn_3P_2 NPs onto (001) Si wafers in a nitrogen-filled glovebox. XRD scans were collected at an incident angle of $\omega = 15°$, unless otherwise noted. Peak fitting (Voigt function) and background subtraction (spline) were performed using Fityk.[93] Peak parameters used for Scherrer analysis (Gaussian fwhm and Lorentzian fwhm) were adjusted for instrumental broadening using a calibrated LaB_6 NIST standard (SRM-660b).

FTIR measurements were performed using a Thermo-Nicolet Nexus 670 FTIR spectrometer in transmission mode. Zn_3P_2 films were deposited on double-side polished silicon wafers purchased from Silicon Valley Microelectronics. TGA measurements were carried out in a nitrogen environment in a Mettler Toledo TGA/DSC1. The nanoparticles were dried under vacuum overnight prior to TGA analysis. A total of 3.235 mg of sample was heated at a rate of 10 °C/min. Film morphology was characterized using a using a Nanoscope IV (Digital Instruments/Veeco) AFM. Imaging was performed in tapping mode, using silicon cantilevers (Nanosensors) having a resonant frequency of 240−280 kHz and a nominal tip radius less than 7 nm.

Optical transmission measurements were performed using a PerkinElmer Lambda 900 spectrometer and Zn_3P_2 films were deposited on quartz substrates. Photoemmission measurements were performed using a Kratos Axis Ultra, equipped with a He Iα photon source ($h\nu$ = 21.2 eV) for UPS and a monochromatic Al Kα X-ray source ($h\nu$ = 1486.6 eV) for XPS. The samples were tilted at a takeoff angle of 90° and the vacuum chamber was at a base pressure of $\sim 10^{-6}$ Torr. Secondary electron cutoff and valence-band UPS measurements were done at biases of −10 and 0 V, respectively. Peak fitting of the Zn($2p_{3/2}$) XPS spectra was done using 7:3 Gaussian−Lorentzian functions. The P(2p) region was fit using 3:7 Gaussian−Lorentzian functions, with the doublet area ratio constrained 2:1 and doublet separation fixed at 0.83 eV.[80]

LbL Film Deposition. All steps of Zn_3P_2 film deposition were performed in a nitrogen-filled glovebox. Films are deposited *via* spin-coating, using either EDT or thermal treatments. First, a layer of Zn_3P_2 NPs was deposited on the desired substrate from a colloidal solution (~40 mg/mL) at 1500 rpm for 20 s. For EDT treatment, the film was then flooded with a solution of EDT/MeOH (10% v/v) and allowed to soak for 10 s, then spun at 1500 rpm for 20 s. Following EDT treatment the film was rinsed with MeOH then octane, where the film was soaked for 5 s then spun at 1500 rpm for 20 s. Following this, another layer of Zn_3P_2 NPs was deposited, then treated with EDT/MeOH and rinsed with MeOH and octane. This process was repeated until the desired film thickness was achieved. For thermal treatments, the as-deposited Zn_3P_2 layer was annealed for 1 min at 525 °C on a hot plate (Fisher, Isotemp), and then allowed to cool for 1 min on a large metal surface. Subsequent Zn_3P_2 layers are deposited and thermally annealed to reach the desired film thickness.

Device Testing. Photovoltaic device testing was measured in air under AM 1.5G simulated solar irradiation with a xenon solar simulator (Oriel 91191 1000 W). The testing irradiance (100 mW/cm^2) was calibrated against a certified Si reference cell fitted with a KG-5 filter (model PVM624, PV Measurements, Inc.). Current−voltage traces of the devices were characteristics using a Keithley 2400 source meter.

Conflict of Interest: The authors declare no competing financial interest.

Acknowledgment. This work was supported by NSERC, NRC-NINT, and CFI. Li Peng is thanked for TEM imaging. Dr. Richard McCreery is acknowledged for access to the UV−vis spectrometer. Sharon Holtz and Tate Hauger are thanked for deposition of top contacts and device testing. The Alberta Centre for Surface Engineering and Science (ACSES) are thanked for performing UPS and XPS measurements. Lastly, Dr. Kenneth Harris and Dr. Brian Worfolk are thanked for the many fruitful discussions regarding synthesis and device testing.

Supporting Information Available: FTIR spectra of free tri-*n*-octylphosphine, XRD spectra, lattice parameter, and grain size determination of ZnO sol−gel films, *J*−*V* curves and photocycling of ITO/ZnO/MoO_3/Ag and EDT treated Zn_3P_2 NP heterojunction devices, XRD spectra of as-deposited and annealed Zn_3P_2 films and a detailed derivation of the core−shell parameters of the Zn_3P_2 NPs. This material is available free of charge *via* the Internet at http://pubs.acs.org.

REFERENCES AND NOTES

1. Bae, W. K.; Padilha, L. A.; Park, Y.; McDaniel, H.; Robel, I.; Pietryga, J. M.; Klimov, V. I. Controlled Alloying of the Core−Shell Interface in CdSe/CdS Quantum Dots for Suppression of Auger Recombination. *ACS Nano* **2013**, *7*, 3411–3419.
2. Cohn, A. W.; Schimpf, A. M.; Gunthardt, C. E.; Gamelin, D. R. Size-Dependent Trap-Assisted Auger Recombination in Semiconductor Nanocrystals. *Nano Lett.* **2013**, *13*, 1810–1815.
3. Mazumdar, S.; Bhattacharyya, A. J. Dependence of Electron Recombination Time and Light to Electricity Conversion Efficiency on Shape of the Nanocrystal Light Sensitizer. *Energy Environ. Sci.* **2013**, *6*, 1494–1498.
4. Oh, S. J.; Berry, N. E.; Choi, J.; Gaulding, E. A.; Paik, T.; Hong, S.; Murray, C. B.; Kagan, C. R. Stoichiometric Control of Lead Chalcogenide Nanocrystal Solids to Enhance Their Electronic and Optoelectronic Device Performance. *ACS Nano* **2013**, *7*, 2413–2421.
5. Ong, W.; Rupich, S. M.; Talapin, D. V.; McGaughey, A. J. H.; Malen, J. A. Surface Chemistry Mediates Thermal Transport in Three-Dimensional Nanocrystal Arrays. *Nat. Mater.* **2013**, *12*, 410–415.
6. Kim, D. K.; Lai, Y.; Diroll, B. T.; Murray, C. B.; Kagan, C. R. Flexible and Low-Voltage Integrated Circuits Constructed from High-Performance Nanocrystal Transistors. *Nat. Commun.* **2012**, *3*, 1216.
7. Mentzel, T. S.; Wanger, D. D.; Ray, N.; Walker, B. J.; Strasfeld, D.; Bawendi, M. G.; Kastner, M. A. Nanopatterned Electrically Conductive Films of Semiconductor Nanocrystals. *Nano Lett.* **2012**, *12*, 4404–4408.
8. Kramer, I. J.; Sargent, E. H. Colloidal Quantum Dot Photovoltaics: A Path Forward. *ACS Nano* **2011**, *5*, 8506–8514.
9. Genovese, M. P.; Lightcap, I. V.; Kamat, P. V. Sun-Believable Solar Paint. A Transformative One-Step Approach for Designing Nanocrystalline Solar Cells. *ACS Nano* **2012**, *6*, 865–872.
10. Ma, W.; Luther, J. M.; Zheng, H.; Wu, Y.; Alivisatos, A. P. Photovoltaic Devices Employing Ternary PbS_xSe_{1-x} Nanocrystals. *Nano Lett.* **2009**, *9*, 1699–1703.
11. Ma, W.; Swisher, S. L.; Ewers, T.; Engel, J.; Ferry, V. E.; Atwater, H. A.; Alivisatos, A. P. Photovoltaic Performance of Ultrasmall PbSe Quantum Dots. *ACS Nano* **2011**, *5*, 8140–8147.
12. McDonald, S.; Konstantatos, G.; Zhang, S.; Cyr, P.; Klem, E.; Levina, L.; Sargent, E. Solution-Processed PbS Quantum Dot Infrared Photodetectors and Photovoltaics. *Nat. Mater.* **2005**, *4*, 138–U14.
13. Ning, Z.; Zhitomirsky, D.; Adinolfi, V.; Sutherland, B.; Xu, J.; Voznyy, O.; Maraghechi, P.; Lan, X.; Hoogland, S.; Ren, Y.; Sargent, E. H. Graded Doping for Enhanced Colloidal Quantum Dot Photovoltaics. *Adv. Mater.* **2013**, *25*, 1719–1723.
14. Pattantyus-Abraham, A. G.; Kramer, I. J.; Barkhouse, A. R.; Wang, X.; Konstantatos, G.; Debnath, R.; Levina, L.; Raabe, I.; Nazeeruddin, M. K.; Graetzel, M.; et al. Depleted-Heterojunction Colloidal Quantum Dot Solar Cells. *ACS Nano* **2010**, *4*, 3374–3380.
15. Tang, J.; Liu, H.; Zhitomirsky, D.; Hoogland, S.; Wang, X.; Furukawa, M.; Levina, L.; Sargent, E. H. Quantum Junction Solar Cells. *Nano Lett.* **2012**, *12*, 4889–4894.
16. Chen, H.; Lai, C.; Wu, I.; Pan, H.; Chen, I. P.; Peng, Y.; Liu, C.; Chen, C.; Chou, P. Enhanced Performance and Air Stability of 3.2% Hybrid Solar Cells: How the Functional Polymer and CdTe Nanostructure Boost the Solar Cell Efficiency. *Adv. Mater.* **2011**, *23*, 5451–5454.
17. Greaney, M. J.; Das, S.; Webber, D. H.; Bradforth, S. E.; Brutchey, R. L. Improving Open Circuit Potential in Hybrid P3HT:CdSe Bulk Heterojunction Solar Cells *via* Colloidal *tert*-Butylthiol Ligand Exchange. *ACS Nano* **2012**, *6*, 4222–4230.
18. Jasieniak, J.; MacDonald, B. I.; Watkins, S. E.; Mulvaney, P. Solution-Processed Sintered Nanocrystal Solar Cells *via* Layer-by-Layer Assembly. *Nano Lett.* **2011**, *11*, 2856–2864.
19. MacDonald, B. I.; Martucci, A.; Rubanov, S.; Watkins, S. E.; Mulvaney, P.; Jasieniak, J. J. Layer-by-Layer Assembly of Sintered $CdSe_xTe_{1-x}$ Nanocrystal Solar Cells. *ACS Nano* **2012**, *6*, 5995–6004.
20. Yaacobi-Gross, N.; Garphunkin, N.; Solomeshch, O.; Vaneski, A.; Susha, A. S.; Rogach, A. L.; Tessler, N. Combining Ligand-Induced Quantum-Confined Stark Effect with Type II

Heterojunction Bilayer Structure in CdTe and CdSe Nanocrystal-Based Solar Cells. *ACS Nano* **2012**, *6*, 3128–3133.

21. Wadia, C.; Alivisatos, A. P.; Kammen, D. M. Materials Availability Expands the Opportunity for Large-Scale Photovoltaics Deployment. *Environ. Sci. Technol.* **2009**, *43*, 2072–2077.
22. Kriegel, I.; Jiang, C.; Rodriguez-Fernandez, J.; Schaller, R. D.; Talapin, D. V.; da Como, E.; Feldmann, J. Tuning the Excitonic and Plasmonic Properties of Copper Chalcogenide Nanocrystals. *J. Am. Chem. Soc.* **2012**, *134*, 1583–1590.
23. Kriegel, I.; Rodriguez-Fernandez, J.; Da Como, E.; Lutich, A. A.; Szeifert, J. M.; Feldmann, J. Tuning the Light Absorption of $Cu_{1.97}S$ Nanocrystals in Supercrystal Structures. *Chem. Mater.* **2011**, *23*, 1830–1834.
24. Liu, X.; Wang, X.; Zhou, B.; Law, W.; Cartwright, A. N.; Swihart, M. T. Size-Controlled Synthesis of $Cu_{2-x}E$ (E = S, Se) Nanocrystals with Strong Tunable Near-Infrared Localized Surface Plasmon Resonance and High Conductivity in Thin Films. *Adv. Funct. Mater.* **2013**, *23*, 1256–1264.
25. Wu, Y.; Wadia, C.; Ma, W.; Sadtler, B.; Alivisatos, A. P. Synthesis and Photovoltaic Application of Copper(I) Sulfide Nanocrystals. *Nano Lett.* **2008**, *8*, 2551–2555.
26. Bi, Y.; Yuan, Y.; Exstrom, C. L.; Darveau, S. A.; Huang, J. Air Stable, Photosensitive, Phase Pure Iron Pyrite Nanocrystal Thin Films for Photovoltaic Application. *Nano Lett.* **2011**, *11*, 4953–4957.
27. Steinhagen, C.; Harvey, T. B.; Stolle, C. J.; Harris, J.; Korgel, B. A. Pyrite Nanocrystal Solar Cells: Promising, or Fool's Gold? *J. Phys. Chem. Lett.* **2012**, *3*, 2352–2356.
28. Wang, D.; Jiang, Y.; Lin, C.; Li, S.; Wang, Y.; Chen, C.; Chen, C. Solution-Processable Pyrite FeS_2 Nanocrystals for the Fabrication of Heterojunction Photodiodes with Visible to NIR Photodetection. *Adv. Mater.* **2012**, *24*, 3415–3420.
29. Fagen, E. A. Optical-Properties of Zn_3P_2. *J. Appl. Phys.* **1979**, *50*, 6505–6515.
30. Kimball, G. M.; Mueller, A. M.; Lewis, N. S.; Atwater, H. A. Photoluminescence-Based Measurements of the Energy Gap and Diffusion Length of Zn_3P_2. *Appl. Phys. Lett.* **2009**, *95*, 112103.
31. Wyeth, N.; Catalano, A. Spectral Response Measurements of Minority-Carrier Diffusion Length in Zn_3P_2. *J. Appl. Phys.* **1979**, *50*, 1403–1407.
32. Kimball, G. M.; Lewis, N. S.; Atwater, H. A. Mg Doping and Alloying in Zn_3P_2 Heterojunction Solar Cells. *35th IEEE Photovolt. Special. Conf.* **2010**, 1039–1043.
33. Bhushan, M.; Catalano, A. Polycrystalline Zn_3P_2 Schottky-Barrier Solar-Cells. *Appl. Phys. Lett.* **1981**, *38*, 39–41.
34. Nayar, P.; Catalano, A. Zinc Phosphide Zinc-Oxide Heterojunction Solar-Cells. *Appl. Phys. Lett.* **1981**, *39*, 105–107.
35. Hermann, A.; Madan, A.; Wanlass, M.; Badri, V.; Ahrenkiel, R.; Morrison, S.; Gonzalez, C. MOCVD Growth and Properties of Zn_3P_2 and Cd_3P_2 Films for Thermal Photovoltaic Applications. *Sol. Energy Mater. Sol. C* **2004**, *82*, 241–252.
36. Shen, G.; Chen, P.; Bando, Y.; Golberg, D.; Zhou, C. Single-Crystalline and Twinned Zn_3P_2 Nanowires: Synthesis, Characterization, and Electronic Properties. *J. Phys. Chem. C* **2008**, *112*, 16405–16410.
37. Sun, T.; Wu, P. C.; Guo, Z. D.; Dai, Y.; Meng, H.; Fang, X. L.; Shi, Z. J.; Dai, L.; Qin, G. G. Synthesis and Characterization of Zn_3P_2/ZnS Core/Shell Nanowires. *Phys. Lett. A* **2011**, *375*, 2118–2121.
38. Wu, P.; Sun, T.; Dai, Y.; Sun, Y.; Ye, Y.; Dai, L. Novel Type-II Zn_3P_2/ZnO Core/Shell Nanowires: Synthesis, Characteristic, and Photoluminescence Properties. *Cryst. Growth Des.* **2011**, *11*, 1417–1421.
39. Yang, R.; Chueh, Y.; Morber, J. R.; Snyder, R.; Chou, L.; Wang, Z. L. Single-Crystalline Branched Zinc Phosphide Nanostructures: Synthesis, Properties, and Optoelectronic Devices. *Nano Lett.* **2007**, *7*, 269–275.
40. Liu, C.; Dai, L.; You, L. P.; Xu, W. J.; Ma, R. M.; Yang, W. Q.; Zhang, Y. F.; Qin, G. G. Synthesis of High Quality p-Type Zn_3P_2 Nanowires and Their Application in MISFETs. *J. Mater. Chem.* **2008**, *18*, 3912–3914.
41. Shen, G.; Bando, Y.; Golberg, D. Synthesis and Structures of High-Quality Single-Crystalline II_3-V_2 Semiconductors Nanobelts. *J. Phys. Chem. C* **2007**, *111*, 5044–5049.
42. Shen, G.; Chen, P.; Bando, Y.; Golberg, D.; Zhou, C. Bicrystalline Zn_3P_2 and Cd_3P_2 Nanobelts and Their Electronic Transport Properties. *Chem. Mater.* **2008**, *20*, 7319–7323.
43. Shen, G.; Ye, C.; Golberg, D.; Hu, J.; Bando, Y. Structure and Cathodoluminescence of Hierarchical Zn_3P_2/ZnS Nanotube/Nanowire Heterostructures. *Appl. Phys. Lett.* **2007**, *90*, 073115.
44. Shen, G.; Bando, Y.; Hu, J.; Golberg, D. Single-Crystalline Trumpetlike Zinc Phosphide Nanostructures. *Appl. Phys. Lett.* **2006**, *88*, 143105.
45. Buhro, W. Metallo-organic Routes to Phosphide Semiconductors. *Polyhedron* **1994**, *13*, 1131–1148.
46. Green, M.; O'Brien, P. A Novel Metalorganic Route to Nanocrystallites of Zinc Phosphide. *Chem. Mater.* **2001**, *13*, 4500–4505.
47. Miao S.; Yang T.; Hickey G. S.; Lesnyak V.; Rellinghaus B.; Xu J.; Eychmuller A. Emmissive ZnO@Zn_3P_2 Nanocrystals: Synthesis, Optical, and Optoelectronic Properties. *Small* [Online early view]. DOI: 10.1002/smll.201203023.
48. Henkes, A. E.; Schaak, R. E. Trioctylphosphine: A General Phosphorus Source for the Low-Temperature Conversion of Metals into Metal Phosphides. *Chem. Mater.* **2007**, *19*, 4234–4242.
49. Henkes, A. E.; Vasquez, Y.; Schaak, R. E. Converting Metals into Phosphides: A General Strategy for the Synthesis of Metal Phosphide Nanocrystals. *J. Am. Chem. Soc.* **2007**, *129*, 1896.
50. De Trizio, L.; Figuerola, A.; Manna, L.; Genovese, A.; George, C.; Brescia, R.; Saghi, Z.; Simonutti, R.; Van Huis, M.; Falqui, A. Size-Tunable, Hexagonal Plate-like Cu_3P and Janus-like Cu-Cu_3P Nanocrystals. *ACS Nano* **2012**, *6*, 32–41.
51. Chen, Y.; She, H.; Luo, X.; Yue, G.; Peng, D. Solution-Phase Synthesis of Nickel Phosphide Single-Crystalline Nanowires. *J. Cryst. Growth* **2009**, *311*, 1229–1233.
52. Muthuswamy, E.; Savithra, G. H. L.; Brock, S. L. Synthetic Levers Enabling Independent Control of Phase, Size, and Morphology in Nickel Phosphide Nanoparticles. *ACS Nano* **2011**, *5*, 2402–2411.
53. Wang, J.; Johnston-Peck, A. C.; Tracy, J. B. Nickel Phosphide Nanoparticles with Hollow, Solid, and Amorphous Structures. *Chem. Mater.* **2009**, *21*, 4462–4467.
54. Maneeprakorn, W.; Malik, M. A.; O'Brien, P. The Preparation of Cobalt Phosphide and Cobalt Chalcogenide (CoX, X = S, Se) Nanoparticles from Single Source Precursors. *J. Mater. Chem.* **2010**, *20*, 2329–2335.
55. Muthuswamy, E.; Brock, S. L. Oxidation Does Not (Always) Kill Reactivity of Transition Metals: Solution-Phase Conversion of Nanoscale Transition Metal Oxides to Phosphides and Sulfides. *J. Am. Chem. Soc.* **2010**, *132*, 15849–15851.
56. Muthuswamy, E.; Kharel, P. R.; Lawes, G.; Brock, S. L. Control of Phase in Phosphide Nanoparticles Produced by Metal Nanoparticle Transformation: Fe_2P and FeP. *ACS Nano* **2009**, *3*, 2383–2393.
57. Strupeit, T.; Klinke, C.; Kornowski, A.; Weller, H. Synthesis of InP Nanoneedles and Their Use as Schottky Devices. *ACS Nano* **2009**, *3*, 668–672.
58. Drits, V.; Srodon, J.; Eberl, D. XRD Measurement of Mean Crystalline Thickness of Illite and Illite/Smectite: Reappraisal of the Kubler Index and the Scherrer Equation. *Clays Clay Miner.* **1997**, *45*, 461–475.
59. Brown, P. R.; Lunt, R. R.; Zhao, N.; Osedach, T. P.; Wanger, D. D.; Chang, L.; Bawendi, M. G.; Bulovic, V. Improved Current Extraction from ZnO/PbS Quantum Dot Heterojunction Photovoltaics Using a MoO_3 Interfacial Layer. *Nano Lett.* **2011**, *11*, 2955–2961.
60. Luther, J. M.; Law, M.; Song, Q.; Perkins, C. L.; Beard, M. C.; Nozik, A. J. Structural, Optical and Electrical Properties of Self-Assembled Films of PbSe Nanocrystals Treated with 1,2-Ethanedithiol. *Acs Nano* **2008**, *2*, 271–280.
61. Ip, A. H.; Thon, S. M.; Hoogland, S.; Voznyy, O.; Zhitomirsky, D.; Debnath, R.; Levina, L.; Rollny, L. R.; Carey, G. H.;

Fischer, A.; *et al.* Hybrid Passivated Colloidal Quantum Dot Solids. *Nat. Nanotechnol.* **2012**, *7*, 577–582.

62. Jeong, K. S.; Tang, J.; Liu, H.; Kim, J.; Schaefer, A. W.; Kemp, K.; Levina, L.; Wang, X.; Hoogland, S.; Debnath, R.; *et al.* Enhanced Mobility-Lifetime Products in PbS Colloidal Quantum Dot Photovoltaics. *ACS Nano* **2012**, *6*, 89–99.
63. Ning, Z.; Ren, Y.; Hoogland, S.; Voznyy, O.; Levina, L.; Stadler, P.; Lan, X.; Zhitomirsky, D.; Sargent, E. H. All-Inorganic Colloidal Quantum Dot Photovoltaics Employing Solution-Phase Halide Passivation. *Adv. Mater.* **2012**, *24*, 6295–6299.
64. Tang, J.; Kemp, K. W.; Hoogland, S.; Jeong, K. S.; Liu, H.; Levina, L.; Furukawa, M.; Wang, X.; Debnath, R.; Cha, D.; *et al.* Colloidal-Quantum-Dot Photovoltaics using Atomic-Ligand Passivation. *Nat. Mater.* **2011**, *10*, 765–771.
65. Koleilat, G. I.; Wang, X.; Labelle, A. J.; Ip, A. H.; Carey, G. H.; Fischer, A.; Levina, L.; Brzozowski, L.; Sargent, E. H. A Donor-Supply Electrode (DSE) for Colloidal Quantum Dot Photovoltaics. *Nano Lett.* **2011**, *11*, 5173–5178.
66. Tauc, J. Optical Properties and Electronic Structure of Amorphous. *Mater. Res. Bull.* **1968**, *3*, 37.
67. Bhusham, M. Mg Diffused Zinc Phosphide n/p Junctions. *J. Appl. Phys.* **1982**, *53*, 514–519.
68. Pawlikowski, J. Absorption-Edge of Zn_3P_2. *Phys. Rev. B* **1982**, *26*, 4711–4713.
69. Brus, L. A Simple-Model for the Ionization-Potential, Electron-Affinity, and Aqueous Redox Potentials of Small Semiconductor Crystallites. *J. Chem. Phys.* **1983**, *79*, 5566–5571.
70. Jasieniak, J.; Califano, M.; Watkins, S. E. Size-Dependent Valence and Conduction Band-Edge Energies of Semiconductor Nanocrystals. *ACS Nano* **2011**, *5*, 5888–5902.
71. Khanna, P. K.; Singh, N.; More, P. Synthesis and Band-Gap Photoluminescence from Cadmium Phosphide Nanoparticles. *Curr. Appl. Phys.* **2010**, *10*, 84–88.
72. Zdanowicz, W.; Zdanowicz, L. Semiconducting Compounds of A^{II} B^{V} Group. *Annu. Rev. Mater. Sci.* **1975**, *5*, 301–328.
73. Demers, S.; van de Walle, A. Intrinsic Defects and Dopability of Zinc Phosphide. *Phys. Rev. B* **2012**, *85*, 195208.
74. Nelson, A.; Kazmerski, L.; Engelhardt, M.; Hochst, H. Valence-Band Electronic-Structure of Zn_3P_2 as a Function of Annealing as Studied by Synchrotron Radiation Photoemission. *J. Appl. Phys.* **1990**, *67*, 1393–1396.
75. Matsushima, T.; Kinoshita, Y.; Murata, H. Formation of Ohmic Hole Injection by Inserting an Ultrathin Layer of Molybdenum Trioxide Between Indium Tin Oxide and Organic Hole-Transporting Layers. *Appl. Phys. Lett.* **2007**, *91*, 253504.
76. Park, Y.; Choong, V.; Gao, Y.; Hsieh, B.; Tang, C. Work Function of Indium Tin Oxide Transparent Conductor Measured by Photoelectron Spectroscopy. *Appl. Phys. Lett.* **1996**, *68*, 2699–2701.
77. Heo, Y.; Norton, D.; Tien, L.; Kwon, Y.; Kang, B.; Ren, F.; Pearton, S.; LaRoche, J. ZnO Nanowire Growth and Devices. *Mater. Sci. Eng. R* **2004**, *47*, 1–47.
78. Ong, B. S.; Li, C.; Li, Y.; Wu, Y.; Loutfy, R. Stable, Solution-Processed, High-Mobility ZnO Thin-Film Transistors. *J. Am. Chem. Soc.* **2007**, *129*, 2750–2751.
79. Kroeger, M.; Hamwi, S.; Meyer, J.; Riedl, T.; Kowalsky, W.; Kahn, A. Role of the Deep-Lying Electronic States of MoO_3 in the Enhancement of Hole-Injection in Organic Thin Films. *Appl. Phys. Lett.* **2009**, *95*, 123301.
80. Meyer, J.; Shu, A.; Kroeger, M.; Kahn, A. Effect of Contamination on the Electronic Structure and Hole-Injection Properties of MoO_3/Organic Semiconductor Interfaces. *Appl. Phys. Lett.* **2010**, *96*, 133308.
81. Kimball, G. M.; Bosco, J. P.; Mueller, A. M.; Tajdar, S. F.; Brunschwig, B. S.; Atwater, H. A.; Lewis, N. S. Passivation of Zn_3P_2 Substrates by Aqueous Chemical Etching and Air Oxidation. *J. Appl. Phys.* **2012**, *112*, 106101.
82. Kimball, G. M.; Lewis, N. S.; Atwater, H. A. Synthesis and Surface Chemistry of Zn_3P_2. *IEEE Photovolt. Spec. Conf., 33rd.* **2008**, 150–155.
83. Nayak, A.; Banerjee, H. X-ray Photoelectron Spectroscopy of Zinc Phosphide Thin Film. *Appl. Surf. Sci.* **1999**, *148*, 205–210.
84. Myers, C.; Franzen, H.; Anderegg, J. X-ray Photoelectron-Spectra and Bonding in Transition-Metal Phosphides. *Inorg. Chem.* **1985**, *24*, 1822–1824.
85. Elrod, U.; Luxsteiner, M.; Obergfell, M.; Bucher, E.; Schlapbach, L. Surface-Chemistry of Zn_3P_2 Single-Crystals Studied by XPS. *Appl. Phys. B* **1987**, *43*, 197–201.
86. Dutkiewlcz, J. The P−Zn (Phosphorus−Zinc) System. *J. Phase Equilib.* **1991**, *12*, 435–438.
87. Thompson, C. Grain Growth in Polycrystalline Thin Films of Semiconductors. *Interface Sci.* **1998**, *6*, 85–93.
88. Misiewicz, J. Optical and Electrical Investigations of Imperfection Levels in Zn_3P_2. *J. Phys. Chem. Solids* **1989**, *50*, 1013–1022.
89. Necas, D.; Klapetek, P. Gwyddion: An Open-Source Software for SPM Data Analysis. *Cent. Eur. J. Phys.* **2012**, *10*, 181–188.
90. Zhang, L.; Holt, C. M. B.; Luber, E. J.; Olsen, B. C.; Wang, H.; Danaie, M.; Cui, X.; Tan, X.; Lui, V. W.; Kalisvaart, W. P. High Rate Electrochemical Capacitors from Three-Dimensional Arrays of Vanadium Nitride Functionalized Carbon Nanotubes. *J. Phys. Chem. C* **2011**, *115*, 24381–24393.
91. Fleming, S.; Rohl, A. GDIS: A Visualization Program for Molecular and Periodic Systems. *Z. Kristallogr.* **2005**, *220*, 580–584.
92. Kloc, K.; Zdanowicz, W. Growth and Morphology of Zn_3P_2, Cd_3P_2 and Cd_3As_2 Crystals. *J. Cryst. Growth* **1984**, *66*, 451–458.
93. Wojdyr, M. Fityk: A General-Purpose Peak Fitting Program. *J. Appl. Crystallogr.* **2010**, *43*, 1126–1128.